Sensitivity functions of frequency-domain magnetic dipole-dipole systems

Rasmus Juhl Tølbøll[1] and Niels Bøie Christensen[1]

ABSTRACT

The resolution capabilities of airborne electromagnetic (AEM) frequency-domain systems are traditionally analyzed in terms of the footprint, which provides a simple measure of the lateral extent of the earth volume involved in a given measurement. However, considerably more detailed insight into the system resolution capabilities can be obtained by studying the 3D sensitivity distribution as defined by the Fréchet derivatives. A qualitative analysis of the 3D sensitivity distributions for six typical magnetic dipole-dipole configurations demonstrates that the spatial resolution characteristics differ widely and that the optimal coil configuration for practical investigations depends on the expected target characteristics. For all six coil configurations, the 3D sensitivity distributions reveal significant sign changes

downwards and outwards from the center, stressing the necessity of reliable starting models for successful inversion of frequency-domain AEM data. Likewise, the central zone of sensitivity for the in-phase component is always larger than for the quadrature, indicating an inferior lateral resolution of the former. A new sensitivity footprint is defined, based on the at-surface behavior of the sensitivity distribution, simply as the area where the sensitivity is at least 10% of its maximum value. For the vertical coaxial (VCA) coil configuration, the size of the sensitivity footprint in the y-direction (perpendicular to the flight path) is approximately a factor of two larger than in the x-direction (along the flight path), while there is virtually no difference for the horizontal coplanar (HCP) coil configuration. The ratio of the HCP to VCA sensitivity footprint exceeds one in both x- and y-directions, suggesting that the VCA coil configuration has the best lateral resolution.

INTRODUCTION

Airborne electromagnetic (AEM) systems operating in the frequency domain have been used worldwide for more than half a century and for widely varying purposes. These include mapping of saltwater intrusions (Fitterman and Deszcz-Pan, 1998), sea-ice thickness estimation (Liu and Becker, 1990; Kovacs et al., 1995; Reid et al., 2006), groundwater and environmental surveys (Sengpiel, 1988; Beamish, 2002; Siemon et al., 2002; Gabriel et al., 2003; Tølbøll and Christensen, 2006), and near-surface structural geological mapping (Ahl, 2003; Gabriel et al., 2003; Eberle and Siemon, 2006).

Modern frequency-domain AEM systems can be grouped into towed-bird helicopter-borne systems and fixed-wing systems. Conventional towed-bird systems, such as the DIGHEM, HUMMINGBIRD or RESOLVE systems, typically employ up to five coil pairs in horizontal coplanar (HCP) or vertical coaxial (VCA) arrangements with transmitter-receiver separations between 5 and 10 m. The transmitter frequencies extend from a few hundred Hertz to

more than 100 kHz, and the nominal system flight height above ground level is around 30 m. Two examples of special towed bird systems are the AWI mini EM bird system, which is designed especially for sea-ice thickness measurements and has a relatively short transmitter-receiver separation (Hass et al., 2006), and the GEM-2A system, which utilizes a single set of transmitter-receiver coils for multi-frequency operation (Won et al., 2003). Fixed-wing systems exist at present only in a single version operated by the Geological Survey of Finland (GTK). Transmitter and receiver coils are here mounted at the wing-tips of the operating aircraft in a vertical coplanar (VCP) coil geometry at a 21.4 m separation, and only two frequencies of 3.1 and 14.4 kHz are employed (Poikonen et al., 1998).

An insight into the system resolution capabilities is of vital importance in examining and comparing the applicability of different AEM prospecting systems. Resolution capability in the vertical direction can be analyzed preferably through inversion theory analysis tools for 1D models (Huang and Palacky, 1991; Tølbøll and Christensen, 2006). The footprint first presented by Liu and Becker (1990)

is an often-used measure of the lateral resolution capabilities of frequency-domain AEM systems. Using an inductive-limit model (infinite transmitter frequency and/or earth conductivity), they define the footprint as the side length of a square area, centered directly below the transmitter, that contains the induced currents accounting for 90% of the measured secondary magnetic field at the receiver. For a system flight height h of 30 m and a coil separation of 6.5 m, the footprint is calculated to be $3.73h$ and $1.35h$ for HCP and VCA coil geometries, respectively, and it is concluded that the VCA coil geometry may have the best lateral resolution. These results are confirmed by Reid and Vrbancich (2004), who calculate the footprints for a variety of contemporary AEM systems.

An alternative approach for the footprint estimation is taken by Beamish (2003). He defines the footprint in terms of the at-surface characteristic of the electric field induced in a conductive half-space, as the lateral distance from the transmitter to where the amplitude of the induced electric field falls to $1/e$ of its maximum value. With this approach, the receiver position and orientation are not taken into account, and only the two limiting cases of horizontal and vertical magnetic transmitter dipoles need to be considered. The study reveals a quasi-linear behavior of the footprint with system flight height and shows that the footprint for a horizontal magnetic dipole is a factor of 1.3 to 1.5 smaller than for a vertical magnetic dipole.

Reid et al. (2006) suggest an improved footprint definition by considering finite frequencies and conductivities, in which case the induced-current system is no longer confined to a simple surface and furthermore comprises both in-phase (IP) and quadrature (Q) components. For a given half-space model and transmitter frequency, they define the footprint as the side length of the cubic volume, centered beneath the transmitter, which accounts for 90% of the measured secondary magnetic field at the receiver. The field measured by the receiver is calculated as the influence of a current element in the earth on the receiver using Biot-Savart's law and not the full induction. The resulting footprint estimates are found to be considerably larger than the traditional inductive-limit footprints, and the ratios of the in-phase to quadrature footprint sizes are calculated to be between 1.55 and 1.72 for the HCP coil configuration, and between 1.54 and 2.01 for the VCA coil configuration.

A more comprehensive way of describing not only the lateral but also the spatial resolution capabilities of electromagnetic systems is through the study of Fréchet derivatives, or sensitivities (Chave, 1984; McGillevrey and Oldenburg, 1990; Hördt, 1998). These sensitivities, which are basically the partial derivatives of the electromagnetic data with respect to the model parameters, describe how different parts of the earth contribute to the model response, and thus provide deep insight into the details of the spatial resolution capabilities and response characteristics of a given system.

In this paper, we examine the resolution capabilities of frequency-domain AEM systems in terms of the sensitivities defined by the Fréchet derivatives for a homogeneous half-space. First, we give a detailed, qualitative description of the sensitivity distributions for six conventional coil configurations. In each case, the 3D sensitivity distributions are visualized through appropriate cross sections, but relevant sensitivity distributions of lower dimensionality are also presented. Next, we analyze the behavior of the sensitivity distributions as a function of the three controlling parameters, which are transmitter frequency, earth conductivity, and system flight height. Finally, as a simplified bulk measure of sensitivity, we introduce and examine a new footprint estimate based on the at-surface characteristic of the 3D sensitivity distribution. This sensitivity footprint accounts for the full induction between the induced current and the receiver coil, and therefore may be more correct theoretically than the existing footprint estimates.

THEORY

System configurations

Throughout this paper, we approximate the system induction coils by magnetic dipoles. This is a valid approximation since the considered coil separations are large compared to the radius of the coils (Zhang et al., 2000). Furthermore, we restrict ourselves to the limiting cases of axis-oriented magnetic dipoles, i.e., magnetic dipoles oriented along the x-, y-, or z-axis in a standard right-hand Cartesian coordinate system with the z-axis pointing vertically down and the x-axis located at the earth's surface in the vertical transmitter-receiver plane. In this special case, there are, in principle, nine different coil configurations to consider as illustrated in Figure 1. Because of symmetry, the PERyx, PERzx, and PERzy coil configurations are identical to the PERxy, PERxz, and PERyz coil configurations over a 1D earth and can be ignored. Hence, only six unique configurations exist.

For simplicity, we will consider the case of a homogeneous half-space, and assume that the transmitter and receiver are located in the same horizontal plane with a constant 10-m separation. This represents a typical measuring situation.

Magnetic field sensitivities

In the frequency-domain, the 3D sensitivity distribution $\mathbf{S}^{3D}$ for a dipole-dipole configuration is formally given as the dot product of the induced electric field strength from the actual transmitter $\mathbf{E}_{Tx}$, and the induced electric field strength from the receiver, had it functioned as a transmitter $\mathbf{E}_{Rx}$ (McGillivray et al., 1994). Thus,

$$\mathbf{S}^{3D}(\mathbf{r}) = \mathbf{E}_{Tx}(\mathbf{r}_{Tx}, \mathbf{r}) \cdot \mathbf{E}_{Rx}(\mathbf{r}_{Rx}, \mathbf{r}), \quad (1)$$

where $\mathbf{r}$ is the position vector for any point in the half-space and $\mathbf{r}_{Tx}$ and $\mathbf{r}_{Rx}$ describe, respectively, the transmitter and receiver position vectors (see Figure 2). The sensitivities defined by equation 1 are sensitivities for the electromotive force induced in the receiver coil. Sensitivities for the ac-

Figure 1. Coil configurations considered in the study. PERyx, PERzx, and PERzy (gray color) are identical to PERxy, PERxz, and PERyz, respectively, over a 1D earth and therefore are ignored.

tual magnetic field data, which are normally associated with frequency-domain AEM system, can be obtained by integration, which is equivalent to division by $i\omega$ in the frequency domain, where ω is the angular transmitter frequency.

The 3D sensitivities are point sensitivities relating small changes in response to small conductivity changes in infinitesimal earth volumes. The main motivation for studying the 3D sensitivities here is that they provide an important insight into the resolution capabilities of electromagnetic systems. Hence, for a given point in the earth, the 3D sensitivity basically reflects the resolution of the conductivity at this point: the higher the absolute value of the sensitivity, the better resolution, and vice versa. The 3D sensitivity distribution will elucidate important resolution aspects of a particular system such as sign, sensitivity to lateral and vertical conductivity structures, and depth of exploration. In this way, the sensitivities comprise much more information than a simple footprint estimate, which is only a bulk measure of the lateral extent of the earth influencing the measurement.

The definition in equation 1 illustrates that the sensitivity distribution is basically an expression of the electric field distribution. The fundamental behavior of the electric field in a conductive half-space because of elevated magnetic dipoles is described by various authors (e.g., Kovacs et al., 1995; Tølbøll and Christensen, 2002; Beamish, 2003; Yin and Hodges, 2005), and shall not be described in further detail here. However, it is worth noticing that the structure (but not the amplitude) of the induced electrical field for a given coil configuration only depends on the system flight height and the product of transmitter frequency and half-space conductivity (Appendix A). The same properties necessarily apply to the sensitivity distribution. Consequently, its behavior can be analyzed exhaustively as a function of only these two parameters

Implementation

For the practical calculations of the 3D sensitivity distributions, the half-space is first discretized into a regular three-dimensional grid arranged symmetrically below the midpoint of the transmitter and receiver dipoles. Next, the total (primary plus secondary) electric field induced by the actual and the auxiliary transmitter at each node point is calculated. The electric field calculations are done in the quasi-static approximation using standard methods (see Appendix A). Finally, the sensitivity at each node point within the half-space is found as the dot product of the two electrical field strengths according to equation 1.

Sensitivity distributions of lower dimensions can be found by integration of the full 3D sensitivity distribution along relevant axes. In this study, we consider both 2D and 1D sensitivities. To keep integration computation time at a minimum without compromising the accuracy, we perform the sampling along the integration axes according to a hyperbolic sine scheme with the sampling distance increasing away from the center of the system. In each case, the sampling distance is chosen sufficiently small and the integration area sufficiently large to ensure a reliable result. The numerical integration is performed by integrating over 11-points at a time using a closed 11-point formula (Abramowitz and Stegun, 1972, equation 25.4.20), and then adding the values together.

RESULTS

Below, the sensitivity distributions for the six coil geometries considered here are presented and discussed individually. The calculations use a frequency-conductivity product of 500 HzS/m, corre-

sponding to, e.g., a frequency of 25 kHz and a resistivity of 50 Ωm. The transmitter and receiver coils are located at points $(5, 0, -30)$ m and $(-5, 0, -30)$ m, respectively, representing a system flight height of 30 m. The flight direction is assumed to be in the positive x-direction.

For each coil configuration, three color-contoured cross sections through the 3D sensitivity distribution are displayed: (1) a vertical cross section in the xz-plane ($y = 0$ m) over the range $-100 \leq x \leq 100$ m, $0 \leq z \leq 100$ m, (2) a vertical cross section in the yz-plane ($x = 0$ m) over the range $-100 \leq y \leq 100$ m, $0 \leq z \leq 100$ m, and (3) a horizontal cross section in the xy-plane ($z = 0$ m) over the range $-100 \leq x \leq 100$ m, $-100 < y < 100$ m. Combined, these three cross sections (shown schematically in Figure 3) provide an adequate insight into the spatial characteristics of the 3D sensitivity distributions.

Also, the vertical 2D sensitivity distribution in the xz-plane $\mathbf{S}^{2Dxz}$ is shown for each coil configuration. This is found by integration of the full 3D sensitivity distribution along the y-axis, i.e.,

$$\mathbf{S}^{2Dxz} = \int_y \mathbf{S}^{3D} dy, \tag{2}$$

and basically describes the average sensitivity in the lateral y-direction, i.e., perpendicular to the flight direction. Likewise, both the horizontal and vertical 1D sensitivity distributions are presented in the graphical representations. The horizontal 1D sensitivity $\mathbf{S}^{1Dx}$ is found by integration of the 3D sensitivity along the y- and the z-axis, i.e.,

$$\mathbf{S}^{1Dx} = \int_y \int_z \mathbf{S}^{3D} dz dy, \tag{3}$$

and is particularly relevant for understanding response characteristics over narrow conductive anomalies. The vertical 1D sensitivity $\mathbf{S}^{1Dz}$ describes the integrated sensitivity as a function of depth and can be used as an indicator for the theoretical depth of exploration. It is found by integration along the x- and y-axis, i.e.,

$$\mathbf{S}^{1Dz} = \int_x \int_y \mathbf{S}^{3D} dy dx. \tag{4}$$

Both in-phase and quadrature components of the sensitivities are presented for each coil configuration. For comparison, the sensitivi-
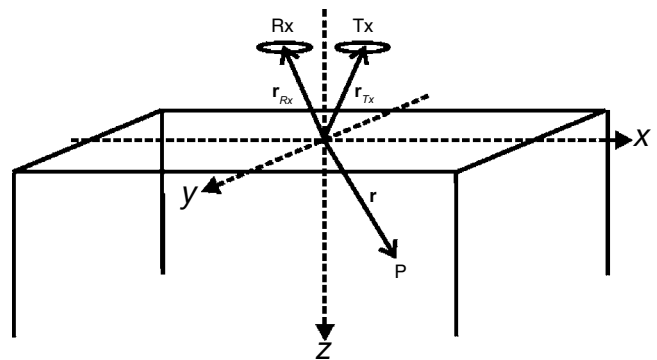

Figure 2. Geometry for calculating the 3D sensitivity at point P. Transmitter (Tx) and receiver (Rx) coils are located in the xz-plane ($y = 0$ m) and the flight direction is along the positive x-direction.

ties are normalized by their maximum sensitivity amplitude, and a nonlinear color-scale is applied in order to cover the sign changes as well as the large dynamic range. The amplitude of the sensitivity S_A, which should not be confused with the sensitivity of the amplitude component, is defined as

$$S_A = \sqrt{(S_I^2 + S_Q^2)}, \qquad (5)$$

where S_I and S_Q denote in-phase and quadrature components of the sensitivity, respectively.

The HCP coil configuration

The sensitivity distribution for the HCP coil configuration is shown in Figure 4. It has an approximately radial symmetric structure with respect to the z-axis and a circular maximum at the surface of the earth. The sensitivity is zero directly underneath both the transmitter and the receiver, which can be understood because the induced electric field underneath a vertical magnetic dipole is identically zero. The volume between the transmitter and the receiver forms a vertical cylindrical structure characterized by negative sensitivity. Likewise, a number of polarity changes, or sign shifts, occur
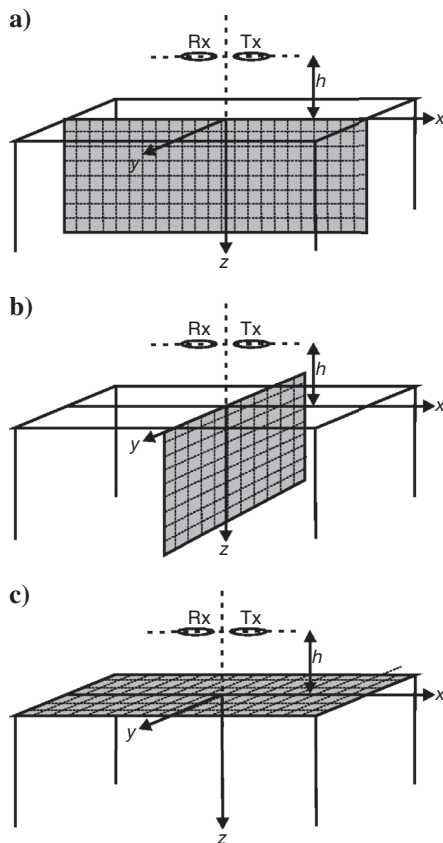

Figure 3. Illustration of cross sections used for visualizing the three-dimensional sensitivity distributions: (a) Vertical section in the xz-plane at $y = 0$ m, (b) vertical section in the yz-plane at $x = 0$ m, and (c) horizontal section in the xy-plane at $z = 0$ m. In all three cases, the transmitter (Tx) and the receiver (Rx) are located in the xz-plane ($y = 0$ m) at a system flight height h above the surface of the earth.

downward and outward from the center. These are caused by varying current flow directions, i.e., the phase changes, and are a general characteristic for EM diffusion phenomena. In the vertical 2D section, the sensitivity between the transmitter and receiver is no longer negative, but a small decrease in intensity and a corresponding upward bulge in the contour lines is still seen nevertheless. This general pattern is reflected in the horizontal 1D sensitivity distribution, which has a positive, symmetrical M-shape with a central localized minimum.

Generally, the symmetric and laterally extended structure of the sensitivity distribution suggests a relatively high sensitivity to vertical conductivity changes and thus a good resolution of horizontal structures. However, it is also clear, especially from the vertical 1D sensitivity distribution, that the relative sensitivity decreases rapidly with depth. Consequently, only near-surface structures can be expected to be reasonably resolved.

The VCA coil configuration

The sensitivity distribution for the VCA coil configuration is displayed in Figure 5. It has a clear bisymmetric structure elongated in the y-direction, and the maximum sensitivity is located in the center of the configuration at the surface of the earth. Two localized minima are found parallel to the flight direction on both sides of the transmitter and the receiver, and sign shifts once again appear both downward and outward from the center.

Compared to the HCP coil configuration, the lateral sensitivity for the VCA coil configurations is considerably more focused along the x-axis, and the contour lines are almost vertical. This suggests a better resolution for vertical conductivity structures striking perpendicular to the flight direction. On the contrary, the contour lines in the y-direction are relatively flat, which means that vertical conductivity structures in this direction are only poorly resolved. By comparison, it is immediately clear that the VCA and the HCP coil configurations have structurally identical 1D sensitivity distributions in the vertical direction. However, in the horizontal direction, the 1D sensitivity distribution for the VCA coil configuration has a simple symmetrical single-spiked shape, which is sharper and better defined compared to the HCP coil configuration.

The VCP coil configuration

For a 1D earth, the 3D sensitivity distribution for the VCP coil configuration is identical to that of the VCA coil configuration except from a 90° rotation around the z-axis. An adequate description can therefore be given based on Figure 5, assuming that the flight direction is now along the positive y-axis.

For obvious reasons, the lateral extent of the sensitivity distribution in the flight direction is considerably larger for the VCP than for the VCA coil configuration. Thus, the capability of resolving vertical conductivity changes perpendicular to the profile line is relatively limited. On the other hand, the sensitivity is highly focused perpendicular to the flight direction, suggesting good resolution capabilities for off-line vertical conductivity changes parallel to the profile line. These properties are utilized by the Finnish fixed-wing system (Poikonen et al., 1998) where the VCP configuration is flown in the y-direction.

The PER*xz* coil configuration

As illustrated in Figure 6, the PER*xz* coil configuration has a relative complicated sensitivity distribution, which basically combines the characteristics of the sensitivity distributions for the HCP and the VCA coil configurations. It is symmetrical only with respect to the *xz*-plane, and seen from above it can be divided into three main areas: a large area of positive sensitivity somewhat in front of the transmitter, another large area of negative sensitivity underneath and behind the transmitter, and finally a small oval area of positive sensitivity just behind the receiver. Directly underneath the receiver, in the vertical direction, the sensitivity is identical zero, which again can be understood because the induced electric field is zero underneath a vertical magnetic dipole.

The complex character of the sensitivity distribution of the PER*xz* coil configuration is clearly reflected in the vertical 2D sensitivity distribution and the horizontal 1D sensitivity distribution, which both have complicated, asymmetrical shapes. Laterally, the resolution capabilities are comparable to the those of the VCA coil configuration, but the extent of the sensitivity distribution along the *x*-axis is considerably larger. In the vertical direction, the 1D sensitivity distribution is virtually similar to those of the preceding coil configurations except for a sign change.

The PER*xy* and PER*yz* coil configuration

As illustrated in Figure 7, the PER*xy* and the PER*yz* coil configurations are special in the sense that their spatial 3D sensitivity distributions are antisymmetrical with respect to the *xz*-plane over a 1D earth. As a consequence, the vertical 2D sensitivity distributions as well as the 1D sensitivity distributions integrate to zero. In the *xz*-plane, the sensitivity functions are identically zero and not shown in the figure.

Because of their antisymmetrical sensitivity distributions, both the PER*xy* and the PER*yz* coil configurations are incapable of resolving vertical resistivity structures that strike perpendicular to the flight direction. On the other hand, they are capable of determining the relative position of vertical conductivity structures, which are asymmetrical with respect to the flight direction.

Frequency, conductivity, and system flight height dependence

Having described the basic shape of the sensitivity distribution, we will now examine its behavior as a function of the frequency-conductivity product and the system flight height. The examination will be based exclusively on the HCP coil configuration, but the overall findings can be extended directly to the remaining coil configurations.

In Figure 8, the vertical cross sections through the 3D sensitivity distribution in the *xz*-plane as well as the vertical 1D sensitivity distributions

are shown for five different frequency-conductivity products between 0.5 and 5000 HzS/m. The system flight height is 30 m, and for each frequency-conductivity product, the associated plots are normalized with respect to their maximum sensitivity amplitude For reference, also a plot showing the theoretical variation of the phase of the secondary magnetic field at the receiver across the considered range of frequency-conductivity products is included. The phase variation is relevant, since it provides information about the relative relevance of the individual in-phase and quadrature components. Thus, low phase values close to 0° indicate that most of the response, and hence also the sensitivity, will be in the in-phase component. High phase values approaching 90° mean that most of the response will be in the quadrature part.

For low frequency-conductivity products, the spatial extent of the sensitivity distribution is found to be relatively high, and most of the sensitivity is located in the quadrature part. However, as the frequency-conductivity product increases, more sensitivity is gradually transferred to the in-phase, and the extent of the sensitivity distribution is decreased dramatically in both the vertical and lateral direction. At the same time, the sensitivities get a more oscillatory charac-
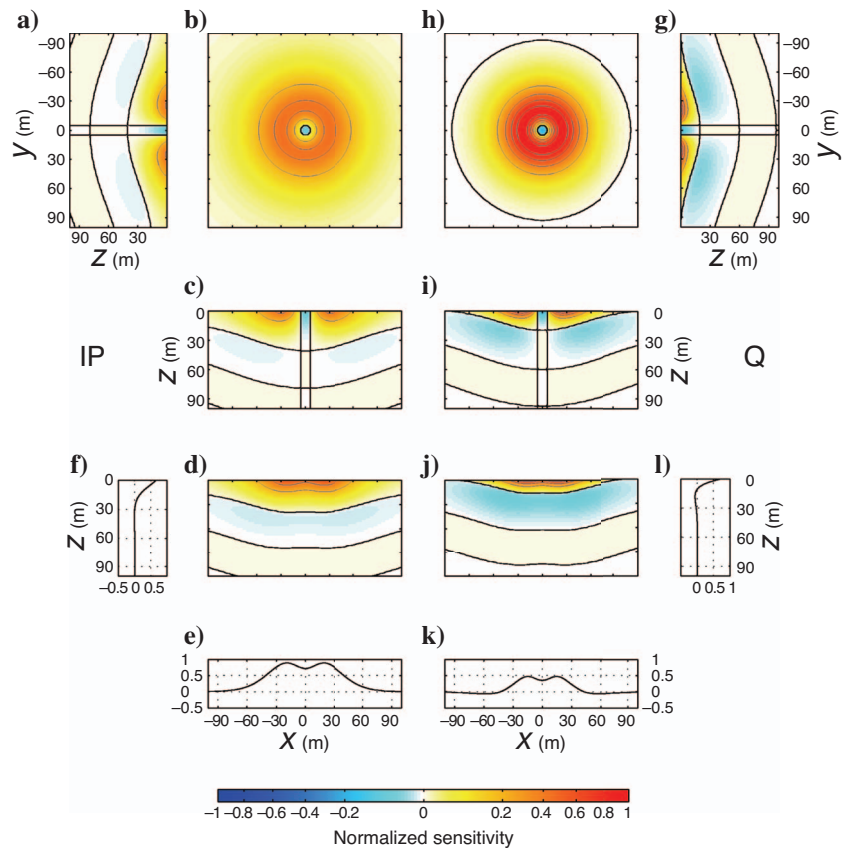

Figure 4. The sensitivity distribution for the HCP coil configuration. Transmitter and receiver coils are located at points $(5,0,-30)$ and $(-5,0,-30)$, respectively, corresponding to a system flight height of 30 m, and the frequency-conductivity product is 500 HzS/m. (a) to (c) Cross sections through the in-phase component of the 3D sensitivity distribution in the vertical *yz*-plane $(x = 0)$, the horizontal *xy*-plane $(z = 0)$, and the vertical *xz*-plane $(y = 0)$, respectively. (d) In-phase component of the vertical 2D sensitivity distribution in the *xz*-plane, and (e) and (f) the in-phase component of the 1D sensitivity distributions along the *x*-axis and the *z*-axis, respectively. (g) to (k) The same except for the quadrature component. In all cases, the sensitivities distributions are normalized with respect to their maximum amplitude. The contour interval is 0.20, and the thick black lines represent transitions from positive to negative sensitivities.

ter because of more closely spaced polarity changes down through the earth, and distinct areas of negative sensitivity start to occur.

From a more general point of view, it is interesting to notice that the spatial extent of the sensitivity distribution is always higher for the in-phase component in comparison with the quadrature component. Also, it appears that the sensitivity is always a maximum at the surface of the earth and decreases relatively fast with the depth.

Figure 9 shows the sensitivity distribution for the HCP coil configuration for five different system flight heights between 10 and 90 m and a fixed frequency-conductivity product of 500 HzS/m. For comparison, the plots are again normalized with respect to the maximum sensitivity amplitude at each system flight height.

As expected, an increase in the system flight height is accompanied by a general increase in the spatial extent of the sensitivity distribution, primarily in the lateral direction. Thus, at the lowest system flight height of 10 m, the principal zone of sensitivity is focused relatively close to the electromagnetic system, but then expands to cover a constantly larger area as the system flight height increases. Despite the fixed frequency-conductivity product, the relative weight of the individual in-phase and quadrature components also changes as the system flight height increases because more weight is gradually given to the in-phase component. This trend is clearly supported by the phase plot, which shows a change from approximately 60° at a system flight height of 10 m to 20° at 100 m. Finally, it shall be mentioned that the absolute sensitivity level drops significantly as the system flight height increases. However, this is not seen in Figure 9 because of the normalization.
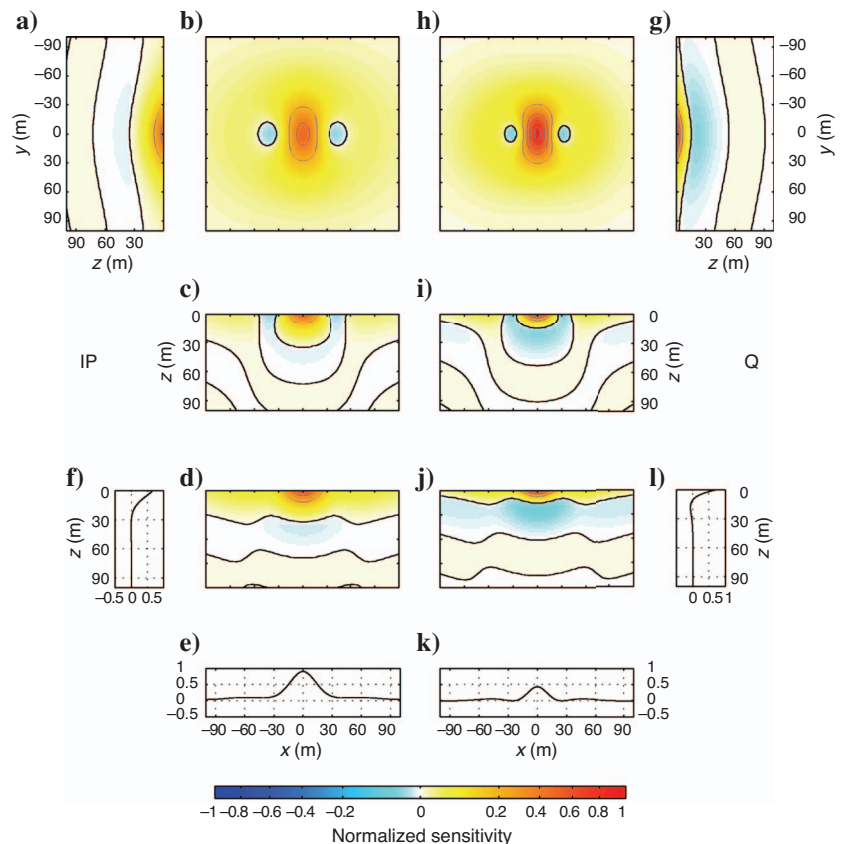
SENSITIVITY FOOTPRINT

From the results presented so far, it is evident that the 3D sensitivity distributions provide detailed insight into the spatial system resolution properties of the magnetic dipole-dipole systems. But because of their complexity, they can be difficult to use directly for simple quantitative, comparative studies. Therefore, it may be useful to define a simple measure for the characteristic size of the sensitivity distributions.

The lateral extent of the 3D sensitivity distribution can be described quantitatively in terms of the traditional footprint terminology. For a given measuring configuration and earth model, it is thus possible to define a sensitivity footprint based on the at-surface behavior of the 3D sensitivity distribution, simply as the area where the sensitivity is at least 10% of its maximum value. This is a reasonable definition, because the sensitivity distribution, as described previously, is always at a maximum at the surface of the half-space, and furthermore, it allows for the calculation of individual in-phase and quadrature footprint estimates.

In Figure 10, the size of the sensitivity footprint is plotted as a function of the frequency-conductivity product for the limiting cases of HCP and VCA coil configurations and a fixed system flight height of 30 m. For both in-phase and quadrature components, the size of the sensitivity footprint is defined by two numbers describing the side lengths of the smallest rectangular bounding box, aligned along the x- and the y-axis, that exactly encloses the calculated sensitivity footprint. A footprint estimate based on the sensitivity amplitude (as defined in equation 5) is shown in Figure 10. Clearly, this sensitivity

Figure 5. The sensitivity distribution for the VCA coil configuration. See Figure 4 for further explanations.

amplitude footprint can be considered as a kind of weighted average that takes the relative relevance of the individual in-phase and quadrature sensitivity footprints into consideration and thus provides a single measure of the effective sensitivity footprint.

As expected from the general shape of the 3D sensitivity distribution (see Figure 4), the sensitivity footprint for the HCP coil configu-

ration has approximately the same size in the x- and the y-direction. In both cases, the quadrature footprint size varies between 160 m ($\sim 5.3h$) and 70 m ($\sim 2.3h$) for the quadrature component, and between more than 500 m (not shown in the figure) and 90 m ($\sim 3.0h$) for the in-phase component. For the VCA coil configuration, the size of the sensitivity footprint is considerably smaller, and it also differs
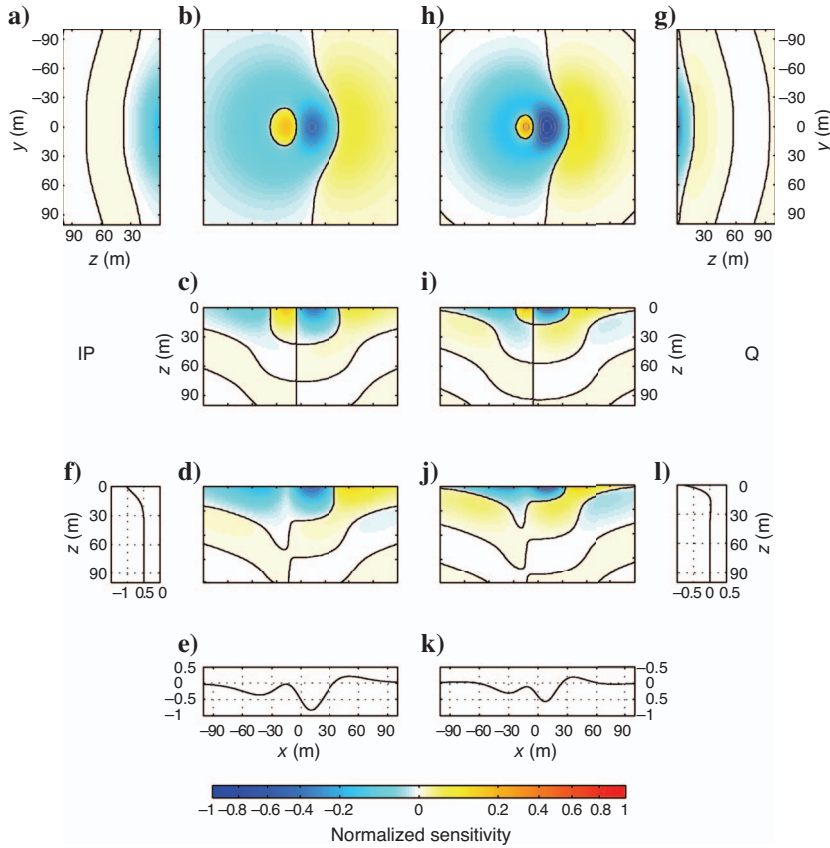

Figure 6. The sensitivity distribution for the PERxz coil configuration. See Figure 4 for further explanations.
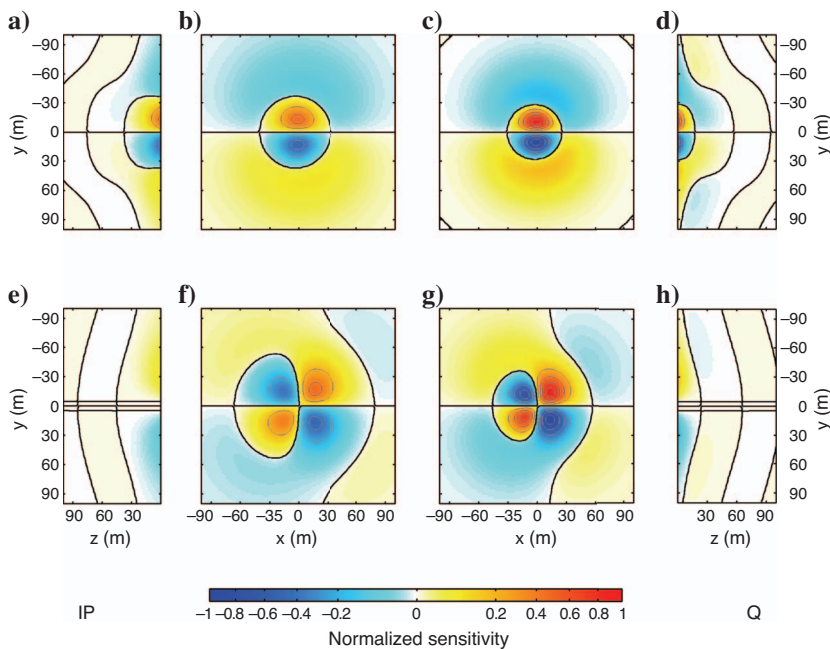

Figure 7. The sensitivity distribution for the PERxy and PERxz coil configurations. Transmitter and receiver coils are located at points $(5,0,-30)$ and $(-5,0,-30)$, respectively, corresponding to a system flight height of 30 m, and the frequency-conductivity product is 500 HzS/m. Cross section through the in-phase component of the 3D sensitivities in (a) the yz-plane ($x = 0$), (b) the xy-plane ($z = 0$), and (c) the xz-plane ($y = 0$). (d-f) are the same but for the quadrature component. The sensitivities are in all cases normalized with respect to the global maximum amplitude. The contour interval is 0.20 and the thick black lines represent transitions from positive to negative sensitivities.

in the x- and y-directions due to the asymmetrical shape of the 3D sensitivity distribution (see Figure 5). For the considered range of frequency-conductivity products, the sensitivity footprint size in the x-direction varies between 59 m ($\sim 2.0h$) and 29 m ($\sim 1.0h$) for the quad-rature component, and between 86 m ($\sim 2.9h$) and 38 m ($\sim 1.3h$) for the in-phase component. In the y-direction, the corre-

sponding values are 112 m ($\sim 3.7h$) and 54 m ($\sim 1.8h$) for the quadrature component and 212 m ($\sim 7.1h$) and 68 m ($\sim 2.3h$) for the in-phase component.

For both the HCP and the VCA coil configuration, the size of the sensitivity amplitude footprint varies gradually from that of the quadrature footprint to that of the in-phase footprint as the value of

Figure 8. The behavior of the sensitivity distribution for the HCP coil configuration for five different frequency-conductivity products between 0.5 and 5000 HzS/m and a fixed system flight height of 30 m. Color-contoured plots represent cross sections through the in-phase (left) and the quadrature (right) component of the 3D sensitivity distribution in the vertical xz-plane, and the graphs in the middle column show the in-phase (red) and the quadrature (blue) component of the vertical 1D sensitivity distribution. For each frequency-conductivity product, the plots are normalized with the maximum. The graph to the far right illustrates the phase of the secondary magnetic field at the receiver.
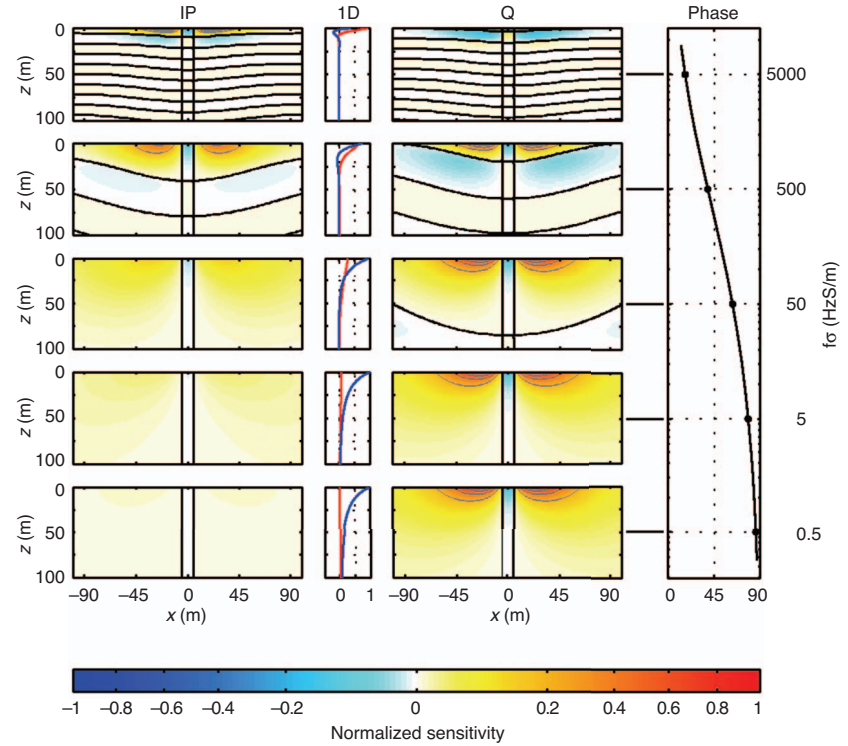

Figure 9. The behavior of the sensitivity distribution for the HCP coil configuration for five different system flight heights between 10 and 90 m and a fixed frequency-conductivity product of 500 HzS/m. Color-contoured plots represent cross sections through the in-phase (left) and the quadrature (right) component of 3D sensitivity distribution in the vertical xz, and the graphs in the middle column show the in-phase (red) and the quadrature (blue) component of the vertical 1D sensitivity distribution. For each frequency-conductivity product, the plots are normalized with the maximum. The graph to the far right illustrates the phase of the magnetic field at the receiver.
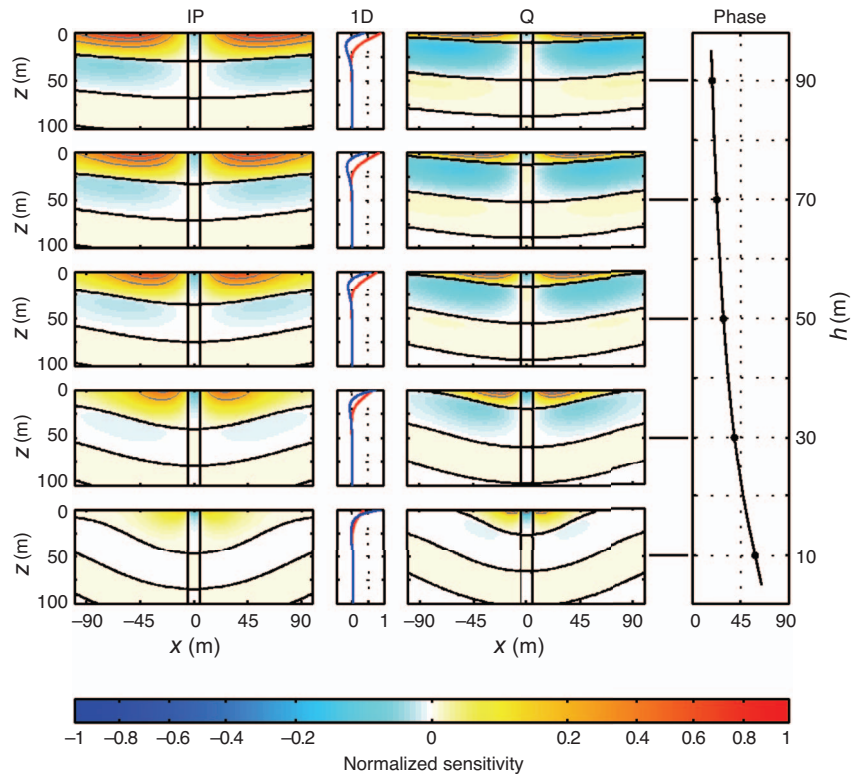
the frequency-conductivity product increases. This is in agreement with the observed variation of the phase of the magnetic field at the receiver, which drops from almost 90° to 0° across the considered interval of frequency-conductivity products (see Figure 10). Based on the sensitivity footprint, it can be concluded that the ratio of the HCP to the VCA footprint size varies between 2.7 and 2.4 in the

x-direction, and between 1.4 and 1.3 in the y-direction across the considered range of frequency-conductivity products. Furthermore, it can be concluded that the footprint in the y-direction is a factor 1.9 to 1.8 larger than in the x-direction for the VCA coil configuration, although they are basically identical for the HCP coil configuration.

In Figure 11, the size of the spatial sensitivity footprint for the
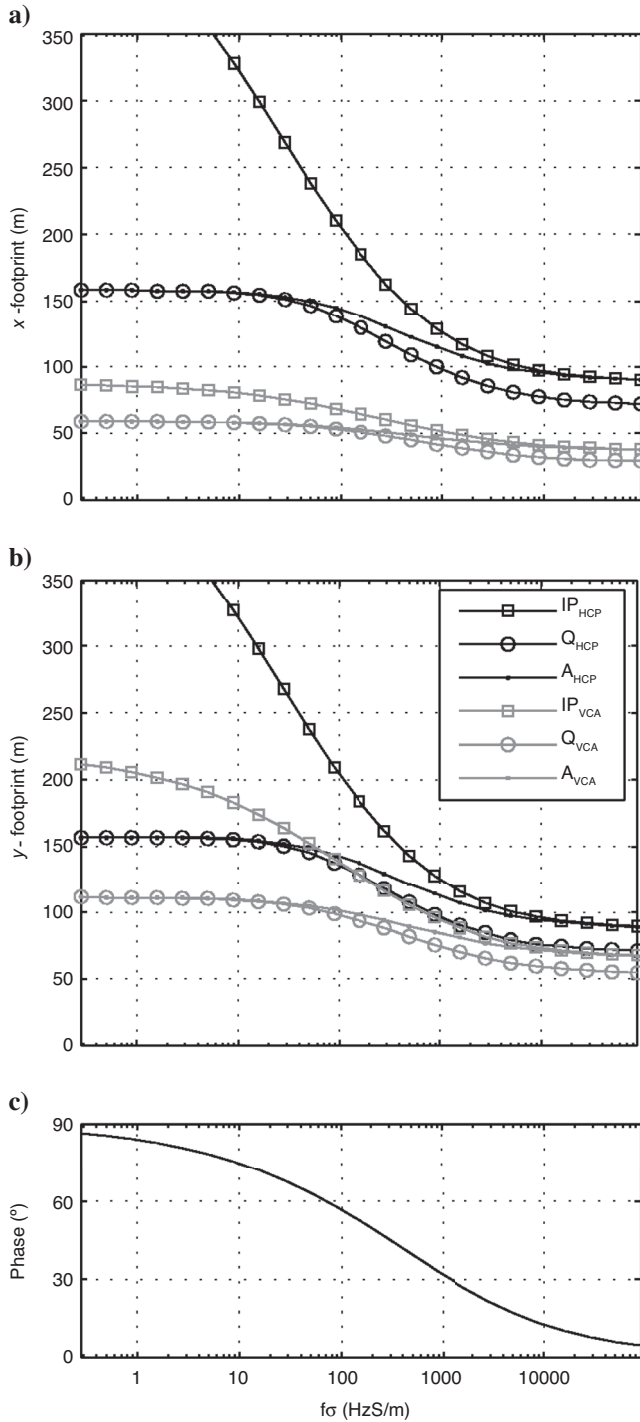

Figure 10. The size of the sensitivity footprint as a function of frequency-conductivity product for the HCP (black) and the VCA (gray) coil configurations in (a) the x-direction and (b) the y-direction. (c) The phase of the secondary magnetic field at the receiver. In all cases, the system flight height is 30 m.
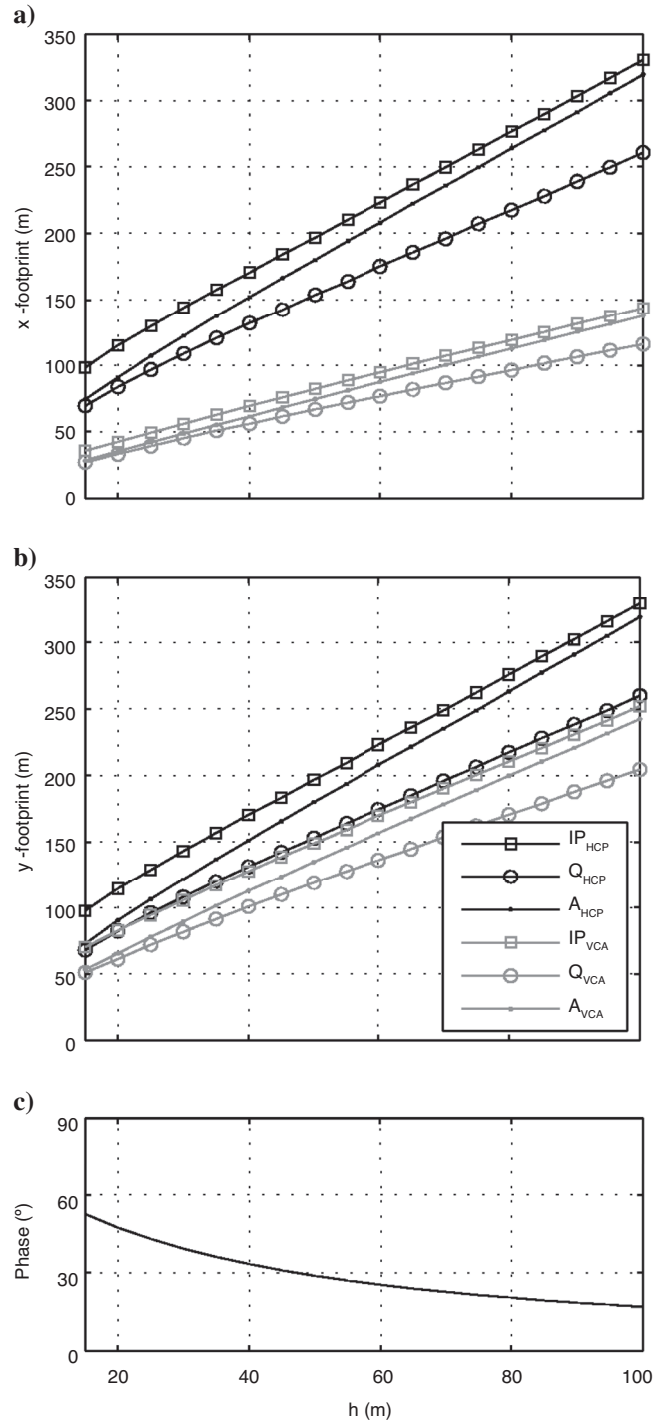
Figure 11. The size of the sensitivity footprint as a function of system flight height for the HCP (black) and the VCA (gray) coil configurations in (a) the x-direction and (b) the y-direction. (c) The phase of the secondary magnetic field at the receiver. In all cases, the frequency-conductivity product is 500 HzS/m.

HCP and the VCA coil configurations is shown for a range of system flight heights between 15 and 90 m and a fixed frequency-conductivity product of 500 HzS/m. From the analysis, it is immediately clear that the size of the sensitivity footprint increases significantly with increased system flight height. The relationship is almost linear, but a tendency towards downward curvature is found at low system flight heights, where the ratio between the transmitter-receiver coil separation and the system flight height becomes relatively high. For the HCP coil configuration, the quadrature sensitivity footprint in both the x- and the y-direction increases from approximately 70 m ($\sim 4.7h$) to 260 m ($\sim 2.6h$) over the considered system flight height range. The corresponding values for the in-phase component are 98 m ($\sim 6.3h$) and 330 m ($\sim 3.3h$). The sensitivity footprint sizes are considerably smaller for the VCA coil configuration. In this case, the quadrature sensitivity footprint size varies between 27 m ($\sim 1.8h$) and 116 m (~ 1.2) in the x-direction, and between 51 m ($\sim 3.4h$) and 205 m ($\sim 2.1h$) in the y-direction. For the in-phase component, the corresponding values are 36m ($\sim 2.4h$) and 144 m ($\sim 1.4h$) in the x-direction and 70 m ($\sim 4.7h$) and 252 m ($\sim 2.5h$) in the y-direction. Finally, the amplitude footprint indicates that the ratio of the HCP to the VCA footprint size varies between 2.6 and 2.3 in the x-direction, and between 1.4 and 1.3 in the y-direction. It also indicates that the footprint for the VCA coil configuration is a factor 1.9 to 1.8 larger in the x-direction than in the y-direction.

DISCUSSION

Sensitivity distributions

Results from the presented study clearly demonstrate that the complexity of the 3D sensitivity distributions for the considered coil configurations increases as HCP $<$ VCA/VCP $<$ PERxz $<$ PERxy/PERyz. Thus, the HCP coil configuration is radically symmetric with respect to the z-axis, the VCA and the VCP coil configurations are bisymmetrical with respect to the x- and the y-axis, the PERxz coil configuration is symmetrical with respect only to the x-axis, and the PERxy/PERyz coil configurations are antisymmetrical with respect to the x-axis. The VCA and the VCP coil configurations are identical except for a 90° rotation around the z-axis. For both the PERxy and the PERyz coil configuration, the 1D and 2D sensitivity distributions are identical zero because of the antisymmetrical shape of the 3D sensitivity distributions.

For all coil configurations, the 3D sensitivity distributions are characterized by a number of sign shifts occurring downward and outward from the center. These shifts, which reflect the varying

phase of the currents, become constantly more closely spaced as the transmitter frequency and/or earth conductivity increases, and explain why reliable starting models are required for successful inversion of frequency-domain AEM data. Furthermore, the central zone of sensitivity is always larger for the in-phase component compared to its quadrature counterpart. This is an important characteristic because it demonstrates that the resolution capabilities are theoretically better for the quadrature component compared to the in-phase component.

Sensitivity footprint

The behavior of the sensitivity footprint as a function of frequency-conductivity product and system flight height can be summarized as follows:

1) For both the HCP and the VCP coil configuration, the sensitivity footprint for the in-phase component is large compared to that of the quadrature, especially at low transmitter frequencies and/or half-space conductivities.
2) The sensitivity amplitude footprint can be used as a weighted footprint estimate that takes the relative relevance of the individual in-phase and quadrature components into consideration.
3) For the VCA coil configuration, the size of the sensitivity amplitude footprint is almost a factor of two larger in the y-direction (perpendicular to the flight path) than in the x-direction (along the flight path), but there is virtually no difference for the HCP coil configuration.
4) The effective ratio of the HCP to VCA sensitivity amplitude footprint is between 2.4 and 2.7 in the x-direction, and between 1.3 and 1.4 in the y-direction.
5) For both the HCP and the VCA coil configuration, the size of the sensitivity footprint increases almost linearly with system flight height, but a downward curvature is observed at low system flight height.

A simple comparison between the sensitivity footprint estimates and the previous influence footprint values of Reid et al. (2006) is illustrated in Table 1, which lists the footprint estimates for the HCP and the VCA coil configuration for a 50 HzS/m frequency-conductivity product and a 30 m system flight height. A good correspondence between the two footprint estimates appears for the VCA coil configuration, but especially for the in-phase component of the HCP coil configuration, the influence footprint is significantly larger than the sensitivity footprint. This discrepancy results from the fact that the influence footprint does not account for the full induction between the current in the earth and the receiver.

CONCLUSIONS

We have analyzed the spatial resolution characteristics of six frequency-domain magnetic dipole-dipole configurations by studying their volumetric sensitivity distributions as defined by the Fréchet derivatives. The results of the study demonstrate that the resolution capabilities vary considerably between the different coil configurations. Each has both advantages and disadvantages, and for practical investigations, the optimal coil configuration depends on the expected target characteristics. Possessing none of the significant details of the sensitivity distribution, a footprint estimate has been defined nevertheless to provide a simple, bulk measure of the lateral extent of the sensitivity distribution. For a given half-space model and mea-

Table 1. Ratio of footprint size versus system flight height for a frequency-conductivity product of 50 Hz S/m and a system flight height of 30 m. Coil separation is 10 m for the sensitivity footprints and 8 m for the influence footprint. Although S_{sensx} and denote the size of the sensitivity footprint size in the x- and y-directions, respectively, S_{infl} is the size of the influence footprint presented by Reid et al. (2006).

	HCP			VCA		
	IP	Q	A	IP	Q	A
	4.8	3.6	4.1	1.9	1.5	1.6
	4.8	3.6	4.1	3.5	2.7	3.0
S_{infl}	5.9	3.7	—	2.5	1.6	—

suring configuration, the footprint is calculated on the basis of at-surface behavior of the 3D sensitivity distribution, as the area where the sensitivity is at least 10% of its maximum value. The new footprint has a high degree of correspondence with previous footprint definitions, and therefore it does not give occasion for a revision of the general conclusions regarding the lateral resolution capabilities. However, the new approach is technically more correct from a theoretical point of view as it accounts for the full induction between the induced current and the receiver, and on a more detailed plane, it actually shows some minor variations.

A selection of animated movies showing the behavior of the sensitivity distribution as a function of the frequency-conductivity product and the system flight height is available for view at www.hgg.dk.

ACKNOWLEDGMENTS

We thank the editor, associate editor, and anonymous reviewers for useful comments and advice.

APPENDIX A

THE ELECTROMAGNETIC FIELD WITHIN A HOMOGENEOUS HALF-SPACE INDUCED BY AN ELEVATED MAGNETIC DIPOLE

In the quasistatic approximation, the total (primary plus secondary) electric field within a homogeneous and isotropic half-space due to a magnetic dipole source can be calculated using standard methods (Ward and Hohmann, 1987). Presented below are equations for a dipole source of moment m located at a system flight height h above the surface of a half-space of conductivity σ.

Vertical magnetic dipole source

For a vertical magnetic dipole source oriented in the positive z-direction, the total electric field within the half-space ($z \geq 0$) is radially symmetric with respect to the z-axis. In cylindrical coordinates, the azimuthal component of the electric field is given by

$$E_{\tilde{\phi}}^{t} = -\frac{i\omega\mu_0 m}{2\pi}\int_0^\infty \frac{\lambda^2}{\lambda + u}e^{-\lambda h}e^{-uz}\mathrm{J}_1(\lambda r)d\lambda, \quad (A\text{-}1)$$

where ω is the angular frequency, μ_0 is the free-space magnetic permeability, λ is the Hankel transform parameter, $u = (\lambda^2 + i\omega\mu_0\sigma)^{1/2}$, and J_1 is the first-order Bessel function. Projection onto the x- and y-axis yields the Cartesian components, i.e.,

$$E_x^{t_z} = -\frac{y}{r}E_{\tilde{\phi}}^{t_z} \text{ and } E_y^{t_z} = \frac{x}{r}E_{\tilde{\phi}}^{t_z}. \quad (A\text{-}2)$$

Horizontal magnetic dipole source

For a horizontal magnetic dipole source in the positive x-direction, the Cartesian components of the total induced electric field within the half-space is given by

$$E_x^{t_x} = \frac{i\omega\mu_0 m}{\pi}\frac{xy}{r^3}\int_0^\infty \frac{\lambda}{\lambda + u}e^{-\lambda h}e^{-uz}\mathrm{J}_1(\lambda r)d\lambda$$

$$-\frac{i\omega\mu_0 m}{2\pi}\frac{xy}{r^2}\int_0^\infty \frac{\lambda^2}{\lambda + u}e^{-\lambda h}e^{-uz}\mathrm{J}_0(\lambda r)d\lambda \quad (A\text{-}3)$$

and

$$E_y^{t_x} = \frac{i\omega\mu_0 m}{2\pi}\left(\frac{1}{r} - \frac{2x^2}{r^3}\right)\int_0^\infty \frac{\lambda}{\lambda + u}e^{-\lambda h}e^{-uz}\mathrm{J}_1(\lambda r)d\lambda$$

$$+\frac{i\omega\mu_0 m}{2\pi}\frac{x^2}{r^2}\int_0^\infty \frac{\lambda^2}{\lambda + u}e^{-\lambda h}e^{-uz}\mathrm{J}_0(\lambda r)d\lambda, \quad (A\text{-}4)$$

where J_0 is the zeroth-order Bessel function.

Likewise, for a horizontal magnetic dipole source in the positive y-direction the total induced electric field is given by

$$E_x^{t_y} = -\frac{i\omega\mu_0 m}{2\pi}\left(\frac{1}{r} - \frac{2y^2}{r^3}\right)\int_0^\infty \frac{\lambda}{\lambda + u}e^{-\lambda h}e^{-uz}\mathrm{J}_1(\lambda r)d\lambda$$

$$-\frac{i\omega\mu_0 m}{2\pi}\frac{y^2}{r^2}\int_0^\infty \frac{\lambda^2}{\lambda + u}e^{-\lambda h}e^{-uz}\mathrm{J}_0(\lambda r)d\lambda \quad (A\text{-}5)$$

and

$$E_y^{y_y} = -\frac{i\omega\mu_0 m}{\pi}\frac{xy}{r^3}\int_0^\infty \frac{\lambda}{\lambda + u}e^{-\lambda h}e^{-uz}\mathrm{J}_1(\lambda r)d\lambda$$

$$+\frac{i\omega\mu_0 m}{2\pi}\frac{xy}{r^2}\int_0^\infty \frac{\lambda^2}{\lambda + u}e^{-\lambda h}e^{-uz}\mathrm{J}_0(\lambda r)d\lambda. \quad (A\text{-}6)$$

Computations

In the general case, the Hankel transforms in equations A-1 to A-6 can only be evaluated by numerical integration. The calculations in this study are performed using the digital filter theory of fast Hankel transforms (Johansen and Sørensen, 1979), and the optimized filter coefficients of Christensen (1990) using a sampling density of 10 per decade.

REFERENCES

Abramowitz, M., and I. A. Stegun, 1972, Handbook of mathematical functions, 9th ed.: National Bureau of Standards.
Ahl, A., 2003, Automatic 1D inversion of multifrequency airborne electromagnetic data with artificial neural networks: Discussion and a case study: Geophysical Prospecting, **51**, 89–97.
Beamish, D., 2002, An assessment of inversion methods for AEM data applied to environmental studies: Journal of Applied Geophysics, **51**, 75–96.
——, 2003, Airborne EM footprints: Geophysical Prospecting, **51**, 49–60.
Chave, A. D., 1984, The Fréchet derivatives of electromagnetic induction:

Journal of Geophysical Research, **89**, 3373–3380.

Christensen, N. B., 1990, Optimized fast Hankel transform filters: Geophysical Prospecting, **38**, 545–568.

Eberle, D. G., and B. Siemon, 2006, Identification of buried valleys using the BGR helicopter-borne geophysical system: Near Surface Geophysics, **4**, 125–133.

Fitterman, D. V., and M. Deszcz-Pan, 1998, Helicopter EM mapping of saltwater intrusion in Everglades National Park, Florida: Exploration Geophysics, **29**, 240–243.

Gabriel, G., R. Kirsch, B. Siemon, and H. Wiederhold, 2003, Geophysical investigation of buried Pleistocene subglacial valleys in Northern Germany: Journal of Applied Geophysics, **53**, 159–180.

Hass, C., J. Lobach, A. Pfaffling, and S. Hendricks, 2006, AWI mini EM bird: Digital technology for sea ice thickness measurements and near surface applications: AEM Workshop Hannover, 2006, Extended Abstracts, 5–7.

Hördt, A., 1998, Calculation of electromagnetic sensitivities in the time domain: Geophysical Journal International, **133**, 713–720.

Huang, H., and G. J. Palacky, 1991, Damped least-squares inversion of time-domain airborne EM data based on singular value decomposition: Geophysical Prospecting, **39**, 827–844.

Johansen, H. K., and K. Sørensen, 1979, Fast Hankel transforms: Geophysical Prospecting, **27**, 876–901.

Kovacs, A., J. S. Holladay, and C. J. J. Bergeron, 1995, The footprint/altitude ratio for helicopter electromagnetic sounding of sea-ice thickness: Comparison of theoretical and field estimates: Geophysics, **60**, 374–380.

Liu, G., and A. Becker, 1990, Two-dimensional mapping of sea-ice keels with airborne electromagnetics: Geophysics, **55**, 239–248.

McGillevrey, P. R., and D. W. Oldenburg, 1990, Methods for calculating Fréchet derivatives and sensitivities for the non-linear inverse problem: A comparative study: Geophysical Prospecting, **38**, 499–524.

McGillivray, P. R., D. W. Oldenburg, R. G. Ellis, and T. M. Habashy, 1994, Calculation of sensitivities for the frequency-domain electromagnetic problem: Geophysical Journal International, **116**, 1–4.

Poikonen, A., K. Sulkanen, M. Oksama, and I. Suppala, 1998, Novel dual frequency fixed wing airborne EM system of Geological Survey of Finland (GTK): Exploration Geophysics, **29**, 46–51.

Reid, J. E., A. Pfaffling, and J. Vrbancich, 2006, Airborne electromagnetic foorprints in 1D earths: Geophysics, **71**, no. 2, G63–G72.

Reid, J. E., and J. Vrbancich, 2004, A comparison of the inductive-limit footprint of airborne electromagnetic configurations: Geophysics, **69**, 1229–1239.

Sengpiel, K.-P., 1988, Approximate inversion of airborne EM data from a multilayered ground: Geophysical Prospecting, **36**, 446–459.

Siemon, B., C. Stuntebeck, K.-P. Sengpiel, B. Röttger, H.-J. Rehli, and D. G. Eberle, 2002, Investigation of hazardous waste sites and their environment using the BGR helicopter-borne geophysical system: Journal of Environmental and Engineering Geophysics, **7**, 169–181.

Tølbøll, R. J., and N. B. Christensen, 2002, The sensitivity functions of airborne frequency domain methods: Proceedings of the 8th Meeting of the EEGS-ES, 539–542.

——, 2006, Robust 1D inversion and analysis of helicopter electromagnetic (HEM) data: Geophysics, **71**, no. 2, G53–G62.

Ward, S. H., and G. W. Hohmann, 1987, Electromagnetic theory for geophysical applications, *in* M. N. Nabighian, ed., Electromagnetic methods in applied geophysics, vol. 1, Theory: SEG Investigations in Geophysics 3, 131–311.

Won, I. J., A. Oren, and F. Funak, 2003, GEM-2A: A programmable broadband helicopter-towed electromagnetic sensor: Geophysics, **68**, 1888–1895.

Yin, C., and G. Hodges, 2005, Four dimensional visualization of EM fields for a helicopter EM system: 75th Annual International Meeting, SEG, Expanded Abstracts, 595–599.

Zhang, Z., P. S. Routh, D. W. Oldenburg, D. L. Alumbaugh, and G. A. Newman, 2000, Reconstruction af 1-D conductivity from dual-loop EM data: Geophysics, **65**, 492–501.